Tunable band structures in digital oxides with layered crystal habits

Yongjin Shin and James M. Rondinelli[*]

Department of Materials Science and Engineering, Northwestern University, Evanston, Illinois 60208, USA

(Received 18 April 2017; revised manuscript received 11 October 2017; published 2 November 2017)

We use density functional calculations to show that heterovalent cation-order sequences enable control over band-gap variations up to several eV and band-gap closure in the bulk band insulator LaSrAlO$_4$. The band-gap control originates from the internal electric fields induced by the digital chemical order, which induces picoscale band bending; the electric-field magnitude is mainly governed by the inequivalent charged monoxide layers afforded by the layered crystal habit. Charge transfer and ionic relaxations across these layers play secondary roles. This understanding is used to construct and validate a descriptor that captures the layer-charge variation and to predict changes in the electronic gap in layered oxides exhibiting antisite defects and in other chemistries.

I. INTRODUCTION

Digital ternary A-B-O oxides consisting of multiple and deliberate periodic cation arrangements are now routinely accessible [1–3]; they can exhibit interesting properties absent from chemically equivalent solid solutions owing to the creation of unique local environments [4]. When the A cations exhibit different formal oxidation states, different internal electric field profiles can be accessed by varying the A cation sequence while maintaining a fixed B-cation valence [5–7]. These electric fields can induce unanticipated electronic, ferroic, and optical functionalities, e.g., two-dimensional electron gases (2DEGs) at oxide heterointerfaces, because the picoscale order produces GV/m fields [8]. The huge internal electric fields cause electrostatic instabilities requiring polarity compensation [9] at the nanoscale, which in oxides is achieved through multiple mechanisms: atomic relaxation [10], charge transfer [11], and vacancy formation [12] or other defects [13]. The long-range chemical order effect is distinct from random heterovalent cation substitution or δ doping in superlattices whereby carriers are introduced into the compound to modulate the charge density [14]. Cation order introduces a complicated interplay among symmetry [15], structure [16,17], electromagnetic interactions [18], and orbital configurations [19] with the balance among these degrees of freedom governing the properties of the digital oxide.

Recently up to 2-eV changes in electronic band gaps were predicted in LaSrAlO$_4$ by changes in the A cation arrangement in the $n = 1$ Ruddlesden-Popper (RP) structure [20]. The A_2BO_4 RP structure consists of alternating perovskite/rocksalt components, $(ABO_3)/(AO)$, stacked along the [001] direction. This layered crystal habit affords stacking of [AO] and [BO_2] layers, which can be utilized to direct the internal electric fields by sequencing of the charged layers: [LaO]$^{1+}$, [SrO]^0, and [AlO$_2$]$^{1-}$. Along with the internal electric fields, electronic band-structure changes are induced by structural bond length and angle distortions in response to the cation order.

Here we realize both semiconducting and metallic LaSrAlO$_4$ at fixed chemical composition by utilizing long period stacking sequences of [LaO]$^{1+}$ and [SrO]^0 layers. We use density functional theory (DFT) calculations to formulate a quantitative model for the band gap variation and collapse, which we show is due to band bending at the subunit cell level. The stacking of charged layers owing to the RP topology makes these ordered oxides natural heterostructures with built-in electric fields. Indeed, we show that the internal electric fields and electrostatic potential profile obtained from DFT can be predicted with a simple ionic model. We then formulate a descriptor which captures the spatial distribution of A cations along the ordering direction, and show its high correlation with the electronic band gap. The descriptor captures a broad range of cation sequences beyond which it was constructed and facilitates prediction of properties sensitive to internal electric fields beyond the band gap.

II. MATERIALS AND METHODS

We constructed 13 unique A cation ordered variants, with ordering along the tetragonal axis (Table I) [21], starting from the bulk LaSrAlO$_4$ structure ($I4/mmm$ symmetry) [22]. A total of eight A-cation sites may be occupied by an equal number of La and Sr to give 70 total variants (including redundant structures), which are reduced down to 13 unique variants by symmetry, including three structures studied in Ref. [20]. Figure 1(a) depicts variant 1, which consists of four different perovskite blocks; its oxide layer sequence along [001] is $\ldots$[SrO-AlO$_2$-SrO] $-$ [SrO-AlO$_2$-LaO] $-$ [LaO-AlO$_2$-LaO] $-$ [LaO-AlO$_2$-SrO]$\ldots$, where "$-$" indicates a separation between the two-dimensional perovskite blocks given in square brackets. The notation can be further simplified by omitting the B cation (Al) and denoting La and Sr as L and S, respectively. Thus variant 1, Fig. 1(a), is defined as SS SL LL LS, such that the A cation pairs now define a perovskite block.

We next performed DFT calculations using the Vienna Ab-initio Simulations Package (VASP) [23,24] with the revised Perdew-Burke-Ernzerhof functional for solids, PBEsol [25], with the plus Hubbard U correction [26]. Projector-augmented wave (PAW) potentials [27] were used to describe the electron core-valence interactions with the following configurations: La ($4f^05s^25p^65d^16s^2$), Sr ($4s^24p^65s^2$), Al ($3s^23p^1$), and O ($2s^22p^4$). A 600-eV plane-wave cutoff is used to obtain the ground structures for each cation variant with $8 \times 8 \times 2$ and $12 \times 12 \times 4$ Monkhorst-Pack k-point meshes [28] for

TABLE I. LaSrAlO$_4$ variants by cation order sequence (S and L denote Sr and La, respectively) and space group (SG). The energy difference relative to the ground state, ΔE, (metal, M, or insulator, I), and energy difference between conduction band (CB, minimum La 5d-orbital energy) and valence band (VB, O maximal 2p-orbital energy) edges, $\varepsilon_{CB} - \varepsilon_{VB}$, are also given for each variant. Negative values indicate metals. Potential-energy differences are calculated between layers with maximum and minimum values from the ionic model (ΔV_{ionic}) and DFT calculations ($\Delta \bar{\bar{V}}_{DFT}$); the latter is for both structures with the ions constrained to the bulk solid-solution structure and with ions relaxed to the ground state. Variant 13 is excluded from calculation of $\Delta \bar{\bar{V}}_{DFT}$ (see Ref. [21]). Variants 9, 12, and 13 correspond to $\eta = 1/2, 2, 1/3$ as referred to in Ref. [20].

Variant	Cation Order	SG	ΔE (eV/f.u.)	State	$\varepsilon_{CB} - \varepsilon_{VB}$ (eV)	ΔV_{ionic} (eV)	$\Delta \bar{\bar{V}}_{DFT}$ (eV)	
							Frozen ions	Relaxed ions
1	SS SL LL LS	$Pmma$	0.492	M	−0.493	−4.73	−10.31	−7.869
2	SS SL LL SL	$P4mm$	0.367	M	−0.135	−3.61	−9.756	−7.278
3	SS SS LL LL	$P4/nmm$	0.558	M	−0.088	−4.06	−10.37	−7.226
4	SS LS LL SL	$Pmma$	0.253	I	0.367	−2.03	−9.109	−6.902
5	SS SL SL LL	$P4mm$	0.271	I	0.380	−3.61	−10.12	−6.794
6	SS SL LS LL	$P4mm$	0.225	I	0.682	−3.04	−9.179	−6.474
7	SS LS SL LL	$P4mm$	0.227	I	0.704	−3.04	−9.391	−6.448
8	SS LS LS LL	$P4mm$	0.180	I	1.055	−1.80	−8.503	−6.233
9	SS LL SS LL	$P4mm$	0.259	I	1.364	−1.35	−7.768	−5.900
10	SL SL LS LS	$P4/nmm$	0.039	I	2.564	−2.70	−7.955	−4.799
11	SL SL SL LS	$P4mm$	0.029	I	2.575	−2.48	−7.925	−4.681
12	SL LS SL LS	$P4/nmm$	0.000	I	3.000	−1.35	−6.734	−4.240
13	SL SL SL SL	$I4mm$	0.024	I	3.149	−0.90		

relaxation and self-consistent total-energy calculations, respectively. Brillouin-zone integrations employed the tetrahedron method [29] for insulating variants and a Gaussian smearing scheme of 50–100 meV for metallic phases. The cell volume and atomic positions were evolved until the forces on each atom were less than 3 meV/Å^{-1}. A Hubbard $U = 10$ eV [30] was applied to the La 4f orbitals to shift the states approximately 6 eV above the Fermi energy [31]. All variants are metastable phases relative to solid solution LaSrAlO$_4$
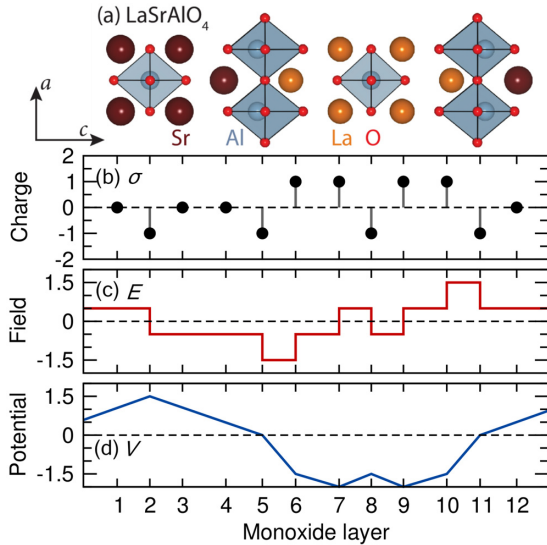

FIG. 1. Equilibrium (a) structure of LaSrAlO$_4$ (metallic variant 1) with its corresponding ionic-model electrostatic quantities (in atomic units); (b) isolated layer charge density (e/a^2), (c) electric field [$\delta E = e/(a^2 \epsilon_0 \epsilon_r)$], and (d) electrostatic potential ($\delta E \, d_{ave}$) along the c axis. The electric-field direction is along the positive c direction.

and are dynamically stable [32]. Detailed structural data are available in Ref. [21], which includes Refs. [33,34].

We used a simple macroscopic average following Ref. [35] with $\bar{\bar{f}}(z) = (1/\alpha) \int_{z-\alpha/2}^{z+\alpha/2} ds \, \bar{f}(s)$, where α is the local period and $\bar{f}(s)$ is the ab planar average of $f(s)$. The determination of the period, α, can be set to the length of building block comprising the disordered bulk structure. This approach then allows us to extract the effective electrostatic potential deviation in the digital superlattices from the disordered structure. For perovskite superlattices, α is routinely set to be the length of a perovskite unit cell which consists of alternating $[AO]$ and $[BO_2]$ layers. In the LaSrAlO$_4$ RP compounds examined, on the other hand, the building block is an isolated 2D perovskite slab, i.e., two $[AO]$ and one $[BO_2]$ layer [36].

III. RESULTS AND DISCUSSION

A. Atomic and electronic structure

Among the 13 variants, cation order produces symmetry reductions from the solid solution (Table I). Only variants 1 and 4 exhibit symmetries lower than that produced by the cation order, i.e., $P4/mmm \rightarrow Pmma$, after achieving dynamic stability. The lowest energy variants are all insulating (see ΔE, Table I) and the highest energy phases, relative to the ground state, exhibit *metallic* behavior. Nonetheless, low-energy variants can be epitaxially stabilized [37] using oxide molecular-beam epitaxy [38,39]. The energetics closely follow the ordering of the charged layers: variants with more chemically equivalent $[AO]$ layers nearby each other are higher in energy.

Beyond affecting phase stability, the inequivalent oxidation states of the cations in the stacked monoxide layers induce considerable variations in the internal electric fields [40] and
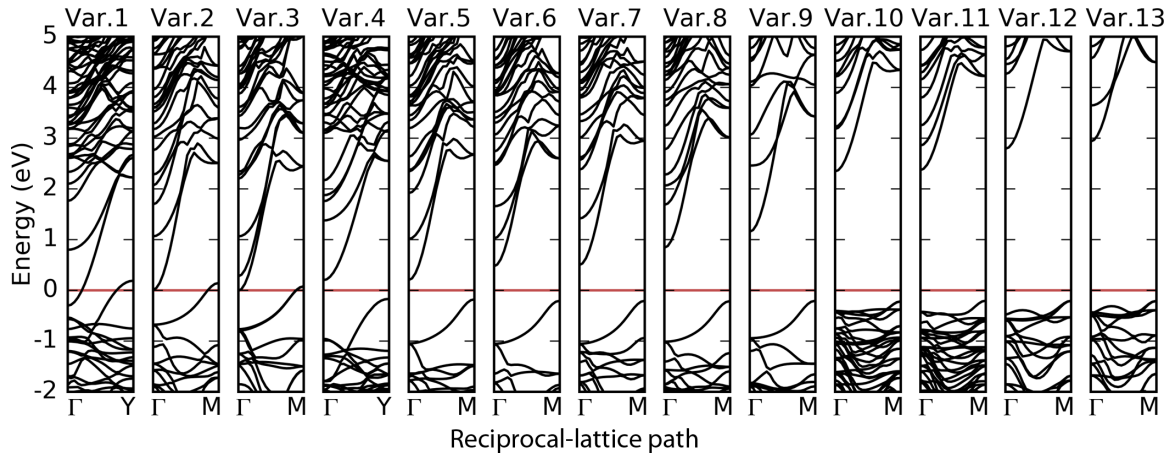
FIG. 2. Band structures for variants 1–13, with the reciprocal space trajectory along the conduction-band minimum and valence-band maximum. The position of the valence-band maximum depends on crystal symmetry: It is located at the M point (1/2, 1/2, 0) for tetragonal variants and Y point (0, 1/2, 0) for orthorhombic variants owing to a zone-folding effect. The Fermi level is located at 0 eV (horizontal, red, line).

electrostatic potential along the ordering axis. Beginning from an ionic model for the superlattice [11], we estimate the electrostatic effect using a layer-averaged charge density (σ) and a parallel-plate capacitor model [13]. The σ values for each $[SrO]^0$, $[AlO_2]^{1-}$, and $[LaO]^{1+}$ are 0, $-e/a^2$, and $+e/a^2$ (in atomic units), respectively, based on the formal oxidation states of the ions. Gauss' law requires a stepwise change in the internal electric field (E) of $\delta E = \sigma/(\epsilon_0 \epsilon_r)$, where ϵ_r is the dielectric constant and the electrostatic potential energy felt by an electron is $V = e \int E dx$. Figure 1 depicts profiles of these electrostatic quantities for variant 1. (Note that we obtain the potential energy in SI units, by using the average layer spacing d_{ave} and ϵ_r of bulk LaSrAlO$_4$ [22], resulting in a conversion factor of 1.35 eV [41].) Despite the fixed chemical composition, V strongly varies with charged monoxide layer sequence: The difference between the largest and smallest layer potential values, ΔV_{ionic}, ranges from -0.90 to -4.73 eV (Table I). We next apply a macroscopic averaging scheme to the local Hartree potential obtained from DFT to determine the internal electric field across each monoxide plane for all variants [35]; the left panel of Fig. 3 depicts the results for variant 1, whereby excellent qualitative agreement is found between the two schemes. Because a larger amplitude of ΔV_{ionic} indicates a larger local electric field within the structure, the electronic properties of the digital oxides with large ΔV_{ionic} are anticipated to deviate from that of the solid solution.

From our DFT calculations, we find that the conduction-band (CB) and valence-band (VB) edges are composed of La 5d and O 2p states, respectively. Figure 2 shows the band structures for all variants along the crystal momentum path defining the band edges. The CB minimum (ε_{CB}) was found at Γ in all variants, where as the VB maximum (ε_{VB}) is located at M or Y, indicating they are indirect gap semiconductors. Remarkably, we find that variants 1–3 among the 13 variants are metallic, i.e., $\varepsilon_{CB} - \varepsilon_{VB} < 0$ (Table I), despite the same LaSrAlO$_4$ composition.

Generally, the electronic density of states (DOS) of variants with large gaps are quite similar while variants with small gaps

have wider bandwidth, especially in the VB [21]. Interestingly, no significant electronic reconstruction occurs. Rather the VB and CB states in each layer-resolved DOS are rigidly shifted, showing a strong correlation to the variation in the local potential profile.

Figure 3 (right) shows a representative metallic case (variant 1). In one $[AlO_2]^{1-}$ layer, the VB edge overlaps with the CB edge of two $[LaO]^{1+}$ layers such that the La 5d and O 2p states cross the Fermi level (E_F), pinning it and producing the insulator-metal transition (IMT). The metallicity is confined to those layers and the Fermi surface reveals a 2DEG [21], similar to SrTiO$_3$/LaAlO$_3$ heterostructures [42], albeit occurring here in a single phase material. In variant 1, the local electric fields obtained from our macroscopic averages range up to 68.8 GV/m, which is $\sim$50% higher than those in the highly insulating variants (e.g., variant 12). This large local electric field enhances the band bending and drives the IMT, as it does at heterojunctions with interface dipoles [43]; however, the band bending here occurs at the subunit cell scale.
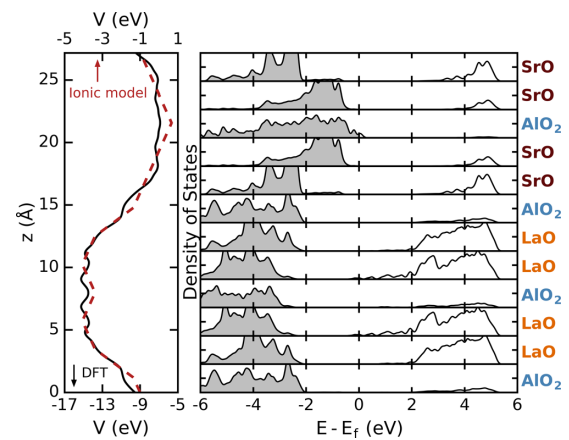

FIG. 3. Averaged electrostatic potential energy (left) from DFT (black, bottom scale) and from the ionic model (red, top scale). Bilayer projected DOS for metallic LaSrAlO$_4$ in variant 1.

The aforementioned interlayer-driven IMT is obtained within a unit cell length of $c \sim 27$ Å, which is considerably shorter than the critical length for the appearance of a 2DEG in $SrTiO_3/LaAlO_3$ heterostructures [42] or head-to-head (tail-to-tail) polarization domain walls in ferroelectric superlattices [44]. We attribute the shorter critical length to arise as direct consequence of the layered RP structure; it permits an additional $[AO]$ monoxide layer for every one perovskite block, providing a route to shorten the distance between different charged layers. Furthermore, the VB character is largely of O $2p$ character; the oxide anion functions then as the necessary electron or hole reservoir and permits so-called self-doping [45].

The cation order dictates the potential profile, which in turn shifts the VB and CB edges, assigned to well-defined oxide layers. Because the band gap is related to the energy difference between the band edges, any shift of the VB/CB edges also provides a measure of the band bending. This observation allows us to define the band bending effect in terms of the local potential differences, $V_{CB} - V_{VB}$, where V_i is the electrostatic potential energy of the CB and VB edge, respectively. This quantity is calculated from both the ionic model as ΔV_{ionic} and at the density functional level as $\Delta \bar{\bar{V}}_{DFT}$ (see Table I). By calculating the shift in the CB/VB edges, the band-gap variation away from the bulk solid-solution structure can be directly quantified. What remains to be determined, however, is how the electrostatic compensation mechanisms, e.g., charge transfer and dielectric screening, affect the equilibrium electrostatic potential profile.

B. Contributions to the band-gap variation

We disentangle these contributions by computing the potential variation relative to the equilibrium band gap using different models (Fig. 4). First, we apply the ionic model such that there is neither charge transfer nor atomic relaxation [21] using the formal oxidization states of the ions. The use of other dynamical [20,46] or chemically motivated [47] charges did not qualitatively affect the results. Across all variants, ΔV_{ionic} captures the general evolution in the band gap with changes in the local potential [Fig. 4(a)]. Next, we obtain the local potential using DFT and calculate $\Delta \bar{\bar{V}}_{DFT}$ for each variant using atomic positions of the solid-solution bulk structure, which we define as the frozen-ion configuration in Fig. 4(b). In this way we capture the effect of charge transfer and chemical bonding independent from the ionic response producing the distribution of oxide-layer spacings. These additional interactions improve the agreement of the linear trend between $\Delta \bar{\bar{V}}_{DFT}$ and the band gap.

We next compute $\Delta \bar{\bar{V}}_{DFT}$ for all variants with the atomic positions fully relaxed, allowing differential ionic displacements, to assess the effect of dielectric screening on these dependencies [Fig. 4(c)]. A more accurate linear trend now emerges, indicating that $\Delta \bar{\bar{V}}_{DFT}$ can be used to understand the band-gap evolution and that it relies on local distortions in the crystal structure. The insets in Fig. 4 depict the two major structural relaxations that occur in response to the local electric field: ionic displacements within a layer (Δu_z, removing the coplanar nature of the cations and oxide ions) and deviations in the interlayer spacing, S. The former occur to
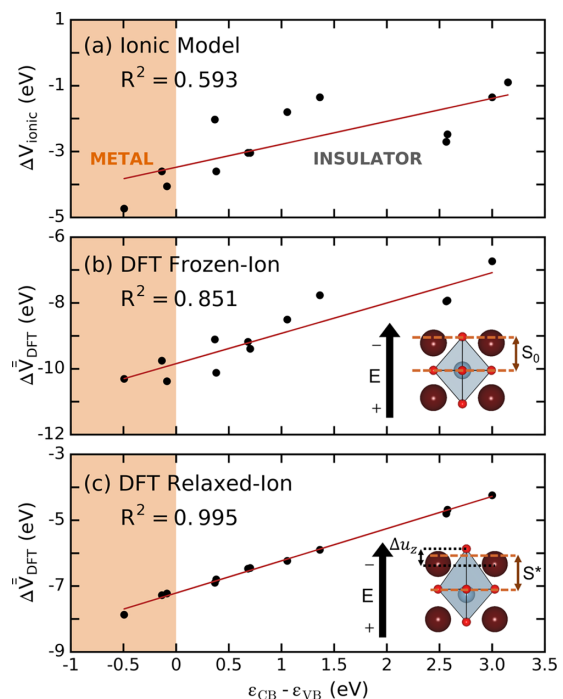

FIG. 4. The potential difference between the CB and VB edges vs $\varepsilon_{CB} - \varepsilon_{VB}$ for all structures using the (a) ionic model, (b) DFT calculations with the solid-solution structure without atomic relaxation, and (c) DFT calculations after atomic relaxation. Macroscopic averaging is applied to the potential-energy profiles computed at the DFT level.

reduce the layer-to-layer potential difference by forming layer polarizations [48]. The layer strains are a result of the interplay among many factors, including bond strength and ionic size: Δu_z and S^* generally decrease with decreasing band gap. Indeed, the largest Δu_z (1.00 Å) and S^* (2.69 Å) were found in the metallic variants 3 and 1, respectively, which deviate from the bulk solid-solution values ($u_z = 0.28$ Å, $S_0 = 2.18$ Å). Higher local electric fields are prominent features of the smaller band-gap oxides ($\varepsilon_{CB} - \varepsilon_{VB} < 1$ eV). This correlation implies these structural contributions evolve to resolve the high electrostatic instability within the structures. Thus, we find that the equilibrium electrostatic potential profile is a result of multiple compensation mechanisms that act to reduce the sharp layer-to-layer gradient (high electric field) in the unit cell.

C. Atomic scale modeling strategy

The general linear evolution and collapse of the band gap with cation order is captured by ΔV_{ionic}. The predictive power of the ionic model motivates us to construct a *structural* descriptor for the explored cation order variants, which can be utilized for electronic structure design of other layered materials. First, we observe that when chemically equivalent $[AO]$ layers are closely clustered, for example in variants 1 and 3 (Table I), the electric field and potential gradients are larger. Therefore, we propose the spatial distribution of A cations, i.e., La and Sr, quantified using a standard deviation σ_A in the z *position* of each A cation, as the band-gap descriptor. Taking the average atomic layer spacing as 2.11 Å, the standard deviation in units of Å provides a sense of the
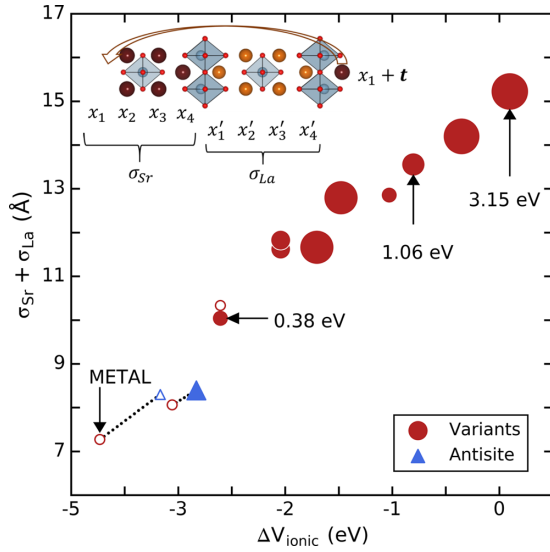
FIG. 5. Sum of the standard deviation of the z position for each A cation depending on the potential difference predicted by the ionic model. The size of each data point represents the relative value of the band gap. Metallic structures are shown as empty symbols. Structures with antisite defects are linked to the corresponding pristine structures by a dotted line.

cation homogeneity over the oxide layers. Noting the periodic boundary conditions of the unit cell, the minimum A cation standard deviations were obtained for each monoxide plane cation X and then summed as

$$\sigma_X = \left[\frac{1}{N} \sum_{i \in X} \{(z_i - \mathbf{t}) - (\bar{z} - \mathbf{t})\}^2 \right]^{1/2},$$

where X and N denote the unique chemical element and the number of X atoms in the unit cell ($N = 4$), respectively, $\bar{z}$ is the mean z position, and $\mathbf{t}$ is an appropriate c-lattice translation for an atom to ensure σ_X is minimized. The resulting standard deviation provides a sense of the cation homogeneity over the oxide layers.

Figure 5 shows the dependence of $\sigma_{Sr} + \sigma_{La}$ on ΔV_{ionic} for each variant with the band gap indicated by the relative size of each symbol. We find a clear linear trend, supporting the model that the A-cation distribution establishes the potential difference in the digital materials and the band-gap evolution. This relationship can be used to predict the relative band gaps of a new chemical composition from a large space of possible digital superlattices; it is especially useful for long periodicities approaching the limits of standard electronic structure methods.

We also address the issue of atomic site mixing in the ordered cation variants and its consequence on the electronic structure. Using LaSrAlO$_4$ variants 1 and 3 as examples, we exchange the La and Sr atoms from their ordered sites at the interface to mimic intermixing [21]. We then recompute the band structure and find a gap opens for variant 3 (0.61 eV) from the metallic state, whereas variant 1 remains metallic despite the site disorder (Fig. 5). The site-occupancy change is captured by our chemical homogeneity descriptor $\sigma_{Sr} + \sigma_{La}$,

which makes it possible to assess how much site intermixing can be tolerated at the nanometer scale before the effect of ordering is reduced. Based on our model predictions, intermixing of A cations will diminish the layer-to-layer variations in the charge density and then the local electric-field strength.

Last we demonstrate the transferability of the ionic model to other systems by performing a similar series of calculations on LaSrBO_4 compounds with $B =$ Ga and Sc [21]. We obtained the same hierarchy of band-gap values depending on the cation order in each variant, supporting the generality of using picoscale variations in the electrostatic potential to control the band gap of digitally ordered materials. Extending the model to layered oxides with d^n B cations is straightforward, however, we note that there may be a more complex interplay of the internal electric field on the band edges owing to Mott and/or charge-transfer physics. Furthermore, the model also applies to materials with A cations of different formal oxidation states, e.g., NaLaTiO$_4$ (Na^{1+} and La^{3+}) and related alkali-metal rare-earth titanates [49]. Indeed, we found similar band-gap variations. Because these layered oxides are proposed anode hosts in the Li-ion battery [6,50], when such oxides are designed with this strategy it may be possible to tune the redox potentials to achieve optimal matching with the electrolytes.

IV. CONCLUSION

In conclusion, we identified that A cation order can tune the electronic band gap in digital oxides with layered habits, making these ordered oxides natural heterostructures. We demonstrated that digital LaSrAlO$_4$ exhibits drastically different properties than the solid solution, namely an insulator-to-metal transition; these metasable superlattices should be accessible via nonequilibrium deposition techniques. The governing principles for the electronic control results from band bending effects driven by variations in the local electrostatic potential. We formulated a point-charge–structure model based on formal oxidation states and the spatial distribution of equivalent A cations to predict the relative size (or collapse) of the band gap, enabling the design of digital oxides in diverse chemistries for photovoltaic or electrochemistry applications; the band gap and metal redox energies may also be predicted prior to synthesis or electronic structure calculations.

ACKNOWLEDGMENTS

[1] B. B. Nelson-Cheeseman, A. B. Shah, T. S. Santos, S. D. Bader, J.-M. Zuo, and A. Bhattacharya, Cation-ordering effects in the single layered manganite $La_{2/3}Sr_{4/3}MnO_4$, Appl. Phys. Lett. **98**, 072505 (2011).

[2] G. Rijnders and D. H. A. Blank, Materials science: Build your own superlattice, Nature (London) **433**, 369 (2005).

[3] J. A. Mundy, C. M. Brooks, M. E. Holtz, J. A. Moyer, H. Das, A. F. Rébola, J. T. Heron, J. D. Clarkson, S. M. Disseler, Z. Liu *et al.*, Atomically engineered ferroic layers yield a room-temperature magnetoelectric multiferroic, Nature (London) **537**, 523 (2016).

[4] T. S. Santos, S. J. May, J. L. Robertson, and A. Bhattacharya, Tuning between the metallic antiferromagnetic and ferromagnetic phases of $La_{1-x}Sr_xMnO_3$ near $x = 0.5$ by digital synthesis, Phys. Rev. B **80**, 155114 (2009).

[5] N. K. Chaki, S. Mandal, A. C. Reber, M. Qian, H. M. Saavedra, P. S. Weiss, S. N. Khanna, and A. Sen, Controlling band gap energies in cluster-assembled ionic solids through internal electric fields, ACS Nano **4**, 5813 (2010).

[6] S.-H. Song, K. Ahn, M. G. Kanatzidis, J. A. Alonso, J.-G. Cheng, and J. B. Goodenough, Effect of an internal electric field on the redox energies of $ALnTiO_4(A = Na \text{ or } Li, Ln = Y \text{ or rare-earth})$, Chem. Mater. **25**, 3852 (2013).

[7] J. Fontcuberta, X. Obradors, and J. B. Goodenough, Influence of internal electric field on the transport properties of the magnetoplumbite system bafe $BaFe_{12-x}Mn_xO_{19}$, J. Phys. C **20**, 441 (1987).

[8] S. Mangin, M. Gottwald, C. H. Lambert, D. Steil, V. Uhlíř, L. Pang, M. Hehn, S. Alebrand, M. Cinchetti, G. Malinowski *et al.*, Engineered materials for all-optical helicity-dependent magnetic switching, Nat. Mater. **13**, 286 (2014); A. Ohtomo and H. Y. Hwang, A high-mobility electron gas at the $LaAlO_3/SrTiO_3$ heterointerface, Nature (London) **427**, 423 (2004); A. M. George, J. Iniguez, and L. Bellaiche, Anomalous properties in ferroelectrics induced by atomic ordering, *ibid.* **413**, 54 (2001); J. Íñiguez and L. Bellaiche, Ab Initio Design of Perovskite Alloys with Predetermined Properties: The Case of $Pb(Sc_{0.5}Nb_{0.5})O_3$, Phys. Rev. Lett. **87**, 095503 (2001); M. Di Stasio, K. A. Müller, and L. Pietronero, Nonhomogeneous Charge Distribution in Layered High-T_c Superconductors, *ibid.* **64**, 2827 (1990).

[9] C. Noguera, Polar oxide surfaces, J. Phys.: Condens. Matter **12**, R367 (2000).

[10] V. Vonk, M. Huijben, K. J. I. Driessen, P. Tinnemans, A. Brinkman, S. Harkema, and H. Graafsma, Interface structure of $SrTiO_3/LaAlO_3$ at elevated temperatures studied *in situ* by synchrotron x rays, Phys. Rev. B **75**, 235417 (2007); S. Okamoto, A. J. Millis, and N. A. Spaldin, Lattice Relaxation in Oxide Heterostructures: $LaTiO_3/SrTiO_3$ Superlattices, Phys. Rev. Lett. **97**, 056802 (2006); M. Huijben, A. Brinkman, G. Koster, G. Rijnders, H. Hilgenkamp, and D. H. A. Blank, Structureproperty relation of $SrTiO_3/LaAlO_3$ interfaces, Adv. Mater. **21**, 1665 (2009); R. Pentcheva and W. E. Pickett, Avoiding the Polarization Catastrophe in $LaAlO_3$ Overlayers on $SrTiO_3(001)$ Through Polar Distortion, Phys. Rev. Lett. **102**, 107602 (2009).

[11] N. Nakagawa, H. Y. Hwang, and D. A. Muller, Why some interfaces cannot be sharp, Nat. Mater. **5**, 204 (2006).

[12] G. Herranz, M. Basletić, M. Bibes, C. Carrétéro, E. Tafra, E. Jacquet, K. Bouzehouane, C. Deranlot, A. Hamzić, J.-M. Broto, A. Barthélémy, and A. Fert, High Mobility in $LaAlO_3/SrTiO_3$ Heterostructures: Origin, Dimensionality, and Perspectives, Phys. Rev. Lett. **98**, 216803 (2007); A. Kalabukhov, R. Gunnarsson, J. Börjesson, E. Olsson, T. Claeson, and D. Winkler, Effect of oxygen vacancies in the $SrTiO_3$ substrate on the electrical properties of the $LaAlO_3/SrTiO_3$ interface, Phys. Rev. B **75**, 121404 (2007).

[13] A. S. Kalabukhov, Yu. A. Boikov, I. T. Serenkov, V. I. Sakharov, V. N. Popok, R. Gunnarsson, J. Börjesson, N. Ljustina, E. Olsson, D. Winkler, and T. Claeson, Cationic Disorder and Phase Segregation in $LaAlO_3/SrTiO_3$ Heterointerfaces Evidenced by Medium-Energy Ion Spectroscopy, Phys. Rev. Lett. **103**, 146101 (2009); L. Yu and A. Zunger, A polarity-induced defect mechanism for conductivity and magnetism at polarnonpolar oxide interfaces, Nat. Commun. **5**, 5118 (2014); Z. Zhong, P. X. Xu, and P. J. Kelly, Polarity-induced oxygen vacancies at $LaAlO_3/SrTiO_3$ interfaces, Phys. Rev. B **82**, 165127 (2010).

[14] H. W. Jang, D. A. Felker, C. W. Bark, Y. Wang, M. K. Niranjan, C. T. Nelson, Y. Zhang, D. Su, C. M. Folkman, S. H. Baek, S. Lee, K. Janicka, Y. Zhu, X. Q. Pan, D. D. Fong, E. Y. Tsymbal, M. S. Rzchowski, and C. B. Eom, Metallic and insulating oxide interfaces controlled by electronic correlations, Science **331**, 886 (2011).

[15] J. M. Rondinelli and C. J. Fennie, Octahedral rotation-induced ferroelectricity in cation ordered perovskites, Adv. Mater. **24**, 1961 (2012).

[16] E. Bousquet, M. Dawber, N. Stucki, C. Lichtensteiger, P. Hermet, S. Gariglio, J.-M. Triscone, and P. Ghosez, Improper ferroelectricity in perovskite oxide artificial superlattices, Nature (London) **452**, 732 (2008).

[17] H. N. Lee, H. M. Christen, M. F. Chisholm, C. M. Rouleau, and D. H. Lowndes, Strong polarization enhancement in asymmetric three-component ferroelectric superlattices, Nature (London) **433**, 395 (2005).

[18] T. Y. Chien, L. F. Kourkoutis, J. Chakhalian, B. Gray, M. Kareev, N. P. Guisinger, D. A. Muller, and J. W. Freeland, Visualizing short-range charge transfer at the interfaces between ferromagnetic and superconducting oxides, Nat. Commun. **4**, 2336 (2013).

[19] V. V. Poltavets, K. A. Lokshin, A. H. Nevidomskyy, M. Croft, T. A. Tyson, J. Hadermann, G. Van Tendeloo, T. Egami, G. Kotliar, N. ApRoberts-Warren, A. P. Dioguardi, N. J. Curro, and M. Greenblatt, Bulk Magnetic Order in a Two-Dimensional $Ni^{1+}/Ni^{2+}(d^9/d^8)$ Nickelate, Isoelectronic with Superconducting Cuprates, Phys. Rev. Lett. **104**, 206403 (2010).

[20] P. V. Balachandran and J. M. Rondinelli, Massive band gap variation in layered oxides through cation ordering, Nat. Commun. **6**, 6191 (2015).

[21] See Supplemental Material at http://link.aps.org/supplemental/10.1103/PhysRevB.96.195108 for additional computational details including crystal structure information, electronic/phonon band structure, density of states, and cation order on other materials systems.

[22] R. D. Shannon, R. A. Oswald, J. B. Parise, B. H. T. Chai, P. Byszewski, A. Pajaczkowska, and R. Sobolewski, Dielectric constants and crystal structures of $CaYAlO_4$, $CaNdAlO_4$, and $SrLaAlO_4$, and deviations from the oxide additivity rule, J. Solid State Chem. **98**, 90 (1992).

[23] G. Kresse and J. Furthmüller, Efficient iterative schemes for *ab initio* total-energy calculations using a plane-wave basis set, Phys. Rev. B **54**, 11169 (1996).

[24] G. Kresse and D. Joubert, From ultrasoft pseudopotentials to the projector augmented-wave method, Phys. Rev. B **59**, 1758 (1999).

[25] J. P. Perdew, A. Ruzsinszky, G. I. Csonka, O. A. Vydrov, G. E. Scuseria, L. A. Constantin, X. Zhou, and K. Burke, Restoring the Density-Gradient Expansion for Exchange in Solids and Surfaces, Phys. Rev. Lett. **100**, 136406 (2008).

[26] S. L. Dudarev, G. A. Botton, S. Y. Savrasov, C. J. Humphreys, and A. P. Sutton, Electron-energy-loss spectra and the structural stability of nickel oxide: An LSDA+U study, Phys. Rev. B **57**, 1505 (1998).

[27] P. E. Blöchl, Projector augmented-wave method, Phys. Rev. B **50**, 17953 (1994).

[28] H. J. Monkhorst and J. D. Pack, Special points for brillouin-zone integrations, Phys. Rev. B **13**, 5188 (1976).

[29] P. E. Blöchl, O. Jepsen, and O. K. Andersen, Improved tetrahedron method for brillouin-zone integrations, Phys. Rev. B **49**, 16223 (1994).

[30] A. I. Liechtenstein, V. I. Anisimov, and J. Zaanen, Density-functional theory and strong interactions: Orbital ordering in Mott-Hubbard insulators, Phys. Rev. B **52**, R5467 (1995).

[31] M. T. Czyżyk and G. A. Sawatzky, Local-density functional and on-site correlations: The electronic structure of La_2CuO_4 and $LaCuO_3$, Phys. Rev. B **49**, 14211 (1994).

[32] W. Sun, S. T. Dacek, S. P. Ong, G. Hautier, A. Jain, W. D. Richards, A. C. Gamst, K. A. Persson, and G. Ceder, The thermodynamic scale of inorganic crystalline metastability, Sci. Adv. **2**, e1600225 (2016).

[33] A. Togo and I. Tanaka, First principles phonon calculations in materials science, Scr. Mater. **108**, 1 (2015).

[34] A. Togo, F. Oba, and I. Tanaka, First-principles calculations of the ferroelastic transition between rutile-type and $CaCl_2$-type SiO_2 at high pressures, Phys. Rev. B **78**, 134106 (2008).

[35] A. Baldereschi, S. Baroni, and R. Resta, Band Offsets in Lattice-Matched Heterojunctions: A Model and First-Principles Calculations for GaAs/AlAs, Phys. Rev. Lett. **61**, 734 (1988).

[36] We note that an incorrect choice of the integration window would significantly disrupt the interpretation of macroscopic average result: a small window will not reduce the fluctuations in the atomic potential and a large window close to unit cell length will make the profile flat without any meaningful information. Fluctuations are commonly found when computing macroscopic averages of the potential profile in the vicinity of a heterointerface (see Fig. 2 of Ref. [42]) due to a change in the layer periodicity. As the proposed cation ordered materials exhibit essential numerous heterointerfaces of this type, minor fluctuations are inevitable. These fluctuations suggest that the macroscopic averaging approach should be used cautiously when drawing conclusions about their internal electric fields since derivatives of the potential profile will also be prone to significant fluctuation.

[37] O. Yu. Gorbenko, S. V. Samoilenkov, I. E. Graboy, and A. R. Kaul, Epitaxial stabilization of oxides in thin films, Chem. Mater. **14**, 4026 (2002).

[38] C. H. Lee, H. Wang, J. A. Mundy, J. Zheng, C. J. Fennie, D. A. Muller, and D. G. Schlom (unpublished).

[39] B. B. Nelson-Cheeseman, H. Zhou, P. V. Balachandran, G. Fabbris, J. Hoffman, D. Haskel, J. M. Rondinelli, and A. Bhattacharya, Polar cation ordering: A route to introducing >10% bond strain into layered oxide films, Adv. Funct. Mater. **24**, 6884 (2014).

[40] J. Goniakowski, F. Finocchi, and C. Noguera, Polarity of oxide surfaces and nanostructures, Rep. Prog. Phys. **71**, 016501 (2008).

[41] In addition to homogeneous dielectric constant and ionic oxidation states, we assumed that all atomic spacings are regarded as uniform, whereby the spacing between the rocksalt layers is about 30% larger than the perovskite interlayer spacing. Anions and cations within the same layer are constrained to have the same z position. C. J. Fall, N. Binggeli, and A. Baldereschi, Deriving accurate work functions from thin-slab calculations, J. Phys.: Condens. Matter **11**, 2689 (1999).

[42] N. C. Bristowe, E. Artacho, and P. B. Littlewood, Oxide superlattices with alternating p and n interfaces, Phys. Rev. B **80**, 045425 (2009).

[43] N. C. Bristowe, P. Ghosez, P. B. Littlewood, and E. Artacho, The origin of two-dimensional electron gases at oxide interfaces: insights from theory, J. Phys.: Condens. Matter **26**, 143201 (2014).

[44] X. Wu and D. Vanderbilt, Theory of hypothetical ferroelectric superlattices incorporating head-to-head and tail-to-tail 180° domain walls, Phys. Rev. B **73**, 020103 (2006).

[45] M. A. Korotin, V. I. Anisimov, D. I. Khomskii, and G. A. Sawatzky, CrO_2: A Self-Doped Double Exchange Ferromagnet, Phys. Rev. Lett. **80**, 4305 (1998).

[46] M. Stengel, Electrostatic stability of insulating surfaces: Theory and applications, Phys. Rev. B **84**, 205432 (2011).

[47] R. F. W. Bader and T. T. Nguyen-Dang, Quantum theory of atoms in molecules–Dalton revisited, Adv. Quantum Chem. **14**, 63 (1981).

[48] S. Hong, S. M. Nakhmanson, and D. D. Fong, Screening mechanisms at polar oxide heterointerfaces, Rep. Prog. Phys. **79**, 076501 (2016).

[49] H. Akamatsu, K. Fujita, T. Kuge, A. Sen Gupta, A. Togo, S. Lei, F. Xue, G. Stone, J. M. Rondinelli, L.-Q. Chen, I. Tanaka, V. Gopalan, and K. Tanaka, Inversion Symmetry Breaking by Oxygen Octahedral Rotations in the Ruddlesden-Popper NaRTiO$_4$ Family, Phys. Rev. Lett. **112**, 187602 (2014).

[50] A. D. Robertson, L. Trevino, H. Tukamoto, and J. T. S. Irvine, New inorganic spinel oxides for use as negative electrode materials in future lithium-ion batteries, J. Power Sources **81–82**, 352 (1999).